BJES Basrah Journal for Engineering Sciences

Basrah Journal for Engineering Sciences, Vol. 25, No. 2, (2025), 1-10

Original Article

Journal homepage: https://bjes.edu.iq/bjes
ISSN (Online): 23118385, ISSN (Print): 18146120

Modelling and Solution of Trapezoidal Variable Orifice Flow Meter: 3D Fluid – Structure Interaction

Rana K. Shamkhi [1]*, Mohammad Ghalambaz [2], Muneer A. Ismael [3]

[1,3] *Department of Mechanical Engineering, College of Engineering, University of Basrah, Basrah, Iraq*
[1] *Al-Ayen Iraqi University, Nasiriyah, Thi-Qar, Iraq*
[2] *Department of Mathematics, Saveetha School of Engineering, SIMATS, Chennai, India*
E-mail addresses: pgs.rana.kareem@uobasrah.edu.iq , m.ghalambaz@gmail.com , muneer.ismael@uobasrah.edu.iq

Article Info

Article history:
Received: 11 April 2025
Revised: 14 June 2025
Accepted: 9 July 2025
Published: 31 December 2025

Keywords:
FSI,
Trapezoidal variable orifice,
Turbulence models.

https://doi.org/10.33971/bjes.25.2.1

Abstract

Gas flow measurements are pivotal in several medical applications. For instance, mechanical ventilators and respiratory monitoring applications need flowmeters with strict requirements. This study is concerned with a three-dimensional computational fluid dynamics (CFD) analysis. The CFD methodology was confirmed by analyzing the flow characteristics of flexible membrane with trapezoidal orifice plates. Variable area orifice meters (VAOMs) are increasingly being embraced in respiratory monitoring applications, employed in the context of mechanical ventilation within medical settings. Each system integrates a flexible orifice plate within the conduit. The simulations are conducted considering realistic deformations in structure through two-way fluid–structure interactions (FSI) using the Arbitrary-Lagrangian–Eulerian (ALE) approach. This research paper analyzes using the finite volume method (FVM). A thorough numerical simulation was performed for the turbulence models. The orifice's thickness and shape significantly influence pressure drop and deflection.

1. Introduction

Accurate and continuous monitoring of gas exchanges during artificial ventilation is pivotal to avoid common side effects related to uncorrected ventilation, such as volutrauma or barotrauma (too high an amount of gas delivered to patients). In this scenario, flowmeters play a crucial role, being used to accurately measure the right amount of gas. Moreover, the volumes of gases exchanged by patients (e.g., minute volume and tidal volume) are estimated by passing the flow signal through an electronic integrator [1]. The respiratory system is essential to living systems. The gas exchange depends on this system, which allows the body to obtain oxygen from the air and eliminate the gases generated as waste by-products in cellular reactions [2]. Flow measurements are essential in mechanical ventilation and in monitoring the respiratory function of patients and athletes [3]. Moreover, flowmeters play a crucial role in the noninvasive assessment of metabolic gas exchange in mechanically ventilated patients via indirect calorimetry [3, 4] and in noninvasive techniques for cardiac output monitoring [4, 5]. Among these systems, orifice meters have several advantages (they are robust, have short response time and good accuracy, and can be designed with minimal volume). The principle of work is based on the presence of an orifice plate within the pipe in which the gas flows. A pressure drop across the plate that non-linearly increases with the flow is the orifice meter output (Bernoulli's law). The non-linear response can be a drawback because the lower the flow rate, the lower the sensitivity [6]. Several patents and studies have been focused on the design of orifice flowmeters with novel geometrical features of the orifice (e.g., fractal-shaped [8] and slotted orifice [7]), but the only solution allowing overcoming the concerns related to their nonlinearity is represented by the design of variable orifice meters (VOMs). Patents based on different configurations (e.g., a flap made of flexible sheet materials like plastic or stainless steel) have been proposed [8-10]. VAOMs allow overcoming the concern related to the nonlinearity of the response of fixed orifice meters or Venturi meters by using specific designs, all based on the same solution: the flow passage area increases with flow. Therefore, the restriction must be designed to allow the mentioned increment (e.g., by using flaps fabricated with flexible materials or other solutions) [11-14]. In addition, the variable orifice flow meter (VOFM) has been developed to reduce expiratory effort and cost. It has gained popularity due to its simplicity, robustness, low manufacturing cost, linear response, and ease of integration with electronic sensors and digital filters. The VOFM offers several advantages, including fast and accurate response, silent operation, and the ability to operate in a wide range of conditions, such as condensation or secretions in the gas flow exhaled by a patient [15]. There are

Several factors on both the performance and the input-output relationship of differential flowmeters, such as restriction design, gas composition, and installation of the primary and secondary element [16-19]. The flexible membrane known as the VOFM, transversely positioned in the respiratory circuit, has one or more trapezoidal plates cut into it. The use of Mylar® (biaxially oriented polyethylene terephthalate) is common in several of the mentioned patents due to its beneficial characteristics such as dimensional stability, flatness, chemical resistance, fatigue resistance, and heat resistance up to 230 °C, good electrical resistance, and

adequate mechanical strength [20-22]. A recent experimental work by Martínez et al. [28] developed a low-cost test rig employing Mylar® plates to quantify how variations in plate length and thickness affect pressure drop across the VOFM, reporting that longer and thinner plates significantly increase sensor sensitivity in both linear and non-linear flow regimes.

This study aims to examine the trapezoidal (VOFM) via mathematical modeling and numerical analysis. We anticipate that the findings of this work will substantially augment the recognized influence of the thickness and cross-sectional area of a VOFM plate on pressure loss.

2. Governing equations

For unsteady, three-dimensional incompressible Newtonian fluid, the governing equations are the Navier-Stokes equations, which include the continuity equation and the momentum conservation equations, given by [23].

Mass conservation equation:

$$\partial\rho + \nabla.(\rho v) = 0 \tag{1}$$

Momentum conservation equation:

$$\frac{\partial}{\partial t}[\rho v] + \nabla.\{\rho vv\} = -\nabla p + \nabla.\{\mu[\nabla v + (\nabla v)^T]\} + f_b \tag{2}$$

That Eqs. (1) and (2) are nonlinear is not by itself an unsurmountable difficulty, since such a problem is usually handled by adopting an iterative approach. Moreover, Eq. (2) is a vector equation, which, when written in terms of its components, results in a system of scalar equations that can be solved sequentially.

3. The geometry of a trapezoidal orifice

Figure 1 illustrates a diagram of a trapezoidal orifice, which was examined in this study. It possesses a thickness of 0.1 millimeters. To ascertain the theoretical mass flow rate of incompressible air traversing a measuring orifice, one employs the Bernoulli equation in conjunction with the continuity equation. The flow of mass determined in this way refers to the flow of perfect, non-sticky fluids, a flow coefficient C was introduced into the theoretical equation for calculating the mass flowrate, which takes into account its reduction. Thus, we obtain the dependence on the actual air mass flowrate. As per the ISO 5167 standard, the fluid mass flowrate qm flowing through the tested trapezoidal orifice can be written by the relationship.

$$q_m = \frac{A_2}{\sqrt{1-\left(\frac{A_2}{A_1}\right)^2}} \cdot \sqrt{2\rho\,\nabla p} \tag{3}$$

Where,

A_1 : is the inlet area of the flowmeter.

A_2 : is the passage area of flow obstruction.

Δp : is the difference pressure before and after the orifice (Pa).

ρ : is the air density (kg/m^3).

$$C = \frac{q_m\sqrt{1-\left(\frac{A_2}{A_1}\right)^4}}{A_1\sqrt{2\rho\,\nabla p}} \tag{4}$$

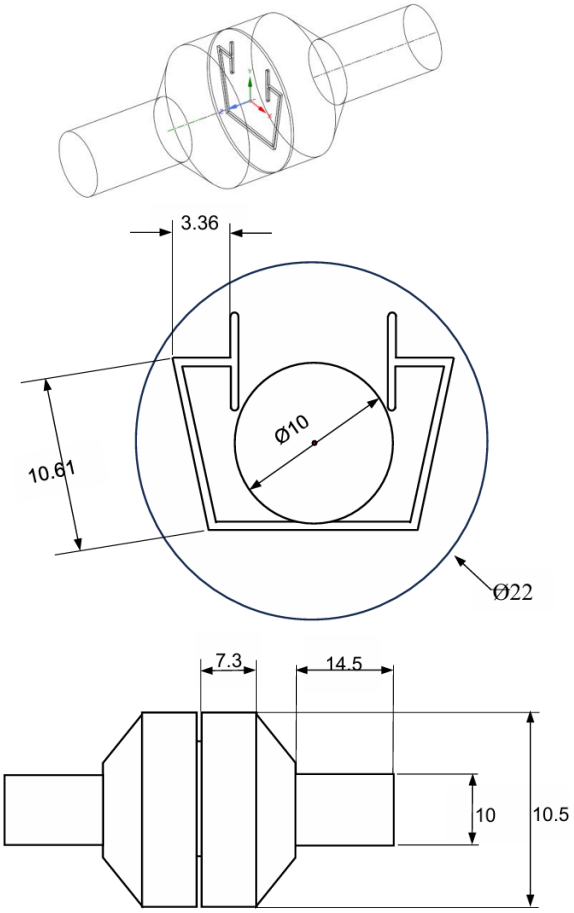

Fig. 1 Geometries and detailed dimensions of a trapezoidal orifice flowmeter.

3.1. Assumptions and boundary conditions

The boundary conditions of the computational domain were as follows:

1. The air is assumed to exhibit Newtonian behavior.
2. Incompressible dry air: with a density of 1.18 kg/m^3.
3. Unsteady and a *k-ω* SST turbulence model has been used for the turbulent.
4. The flexible membranes are made of Mylar sheets have an Elasticity modulus of 2×10^{11} Pa, Young modulus of 5.1×10^8 Pa, density 1390 kg/m^3 and Poisson ratio 0.42.

4. CFD modelling

The flowmeter based on a trapezoidal orifice was subjected to numerical analyses. Simulations were conducted using the Ansys Fluent solver. In the current studies, a three-dimensional (3D) model of a trapezoidal orifice has been developed to analyze the air flow and pressure drop. The mesh was generated in the entire domain, including the upstream and downstream sections of the pipeline. After some of the preliminary tests, a final mesh contained 2,166,010 elements with element size is 0.001 m, was used to guarantee mesh-independent results. The final version of the mesh, is shown in Fig. 2.

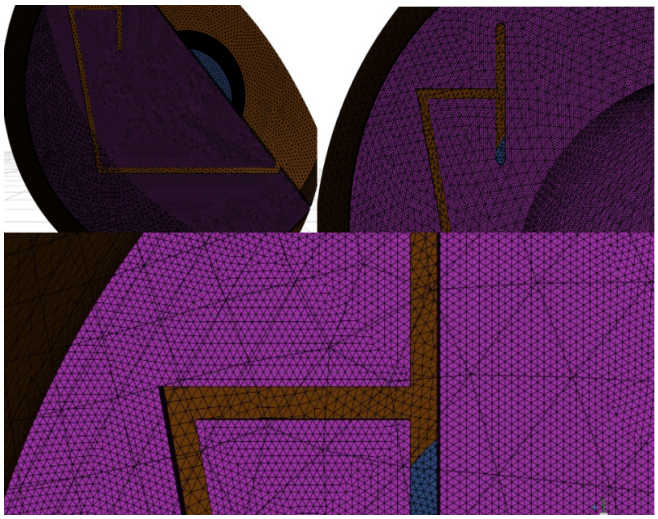

Fig. 2 Tetrahedral element for a trapezoidal variable orifice flow meter.

Two turbulent models were used, the Shear Stress Transport k-ω turbulence model known as *k-ω* SST is used [25]. The *k-ω* SST turbulence model is widely employed in the field of fluid dynamics for accurately forecasting adverse pressure gradient boundary layers and flow separation. The *k-ω* SST model is a combination of the k-ω turbulence model by Wilcox (1988) [26] and the *k-ε* turbulence model created by Launder & Spalding (1972) [27], The objective is to utilize the *k-ω* model for the near-surface areas and the *k-ε* model for the outer boundary layers and free shear layers. The Reynolds momentum equation of the *k-ω* SST model

$$\rho\frac{\partial u_i}{\partial t}+\rho\, u_i\frac{\partial u_i}{\partial x_i}=\rho g_i - \frac{\partial p}{\partial x_i}+\mu\frac{\partial^2 u_j}{\partial x_i\,\partial x_j}+\frac{\partial}{\partial_i}\left[\mu_t\left(\frac{\partial u_j}{\partial x_i}+\frac{\partial u_i}{\partial x_j}\right) -\frac{2}{3}\rho\frac{\partial k}{\partial x_i}\right] \quad (5)$$

In the equations above, k = 0.41 is the turbulence kinetic energy, μ_t is the turbulent viscosity and ϑ_t kinamatic turbulent viscosity

$$\mu_t=\rho\,\vartheta_t \quad , \quad \vartheta_t=\frac{k}{\omega}$$

Where ω specific turbulent dissipation rate, the force terms in the momentum equation provide a link between velocity and pressure.

The turbulent kinetic energy equation of the *k-ω* SST model

$$\rho\frac{\partial k}{\partial t}+\rho u_i\frac{\partial k}{\partial x_i}=\mu_t\left(\frac{\partial u_j}{\partial x_i}+\frac{\partial u_i}{\partial x_j}\right)\frac{\partial u_i}{\partial x_j} - \rho\beta^*\omega k+\frac{\partial}{\partial x_i}\left(\left(\mu+\sigma_k\,\mu_t\right)\frac{\partial k}{\partial x_i}\right) \quad (6)$$

where β^*=0.09 is a constant taken from Wilcox

$$\sigma_k=\sigma_{k1}\,F_1+(1-F_1)\sigma_{k2} \quad (7)$$

$$F_1=tanh\left\{Max\left[Min\frac{\sqrt{k}}{0.09\omega y}0.45\frac{\omega}{|\Omega|}\ \frac{500\,\vartheta}{\omega y^2}\right]^4\right\} \quad (8)$$

In the equations above, y is distance to the next surface, ϑ *is* kinematic viscosity of the fluid and $|\Omega|$ is the magnitude of mean vorticity

$$|\Omega|=\sqrt{\left(\frac{\partial u_3}{\partial x_2}-\frac{\partial u_2}{\partial x_3}\right)^2+\left(\frac{\partial u_1}{\partial x_3}-\frac{\partial u_3}{\partial x_1}\right)^2+\left(\frac{\partial u_2}{\partial x_1}-\frac{\partial u_1}{\partial x_2}\right)^2} \quad (9)$$

The specific dissipation rate equation of the *k-ω* SST model

$$\rho\frac{\partial\omega}{\partial t}+\rho u_i\frac{\partial\omega}{\partial x_i}=\gamma\rho\left(\frac{\partial u_j}{\partial x_i}+\frac{\partial u_i}{\partial x_j}\right)\frac{\partial u_i}{\partial x_j} - \rho\beta\omega^2+\frac{\partial}{\partial x_i}\left[\left(\mu+\sigma_\omega\mu_t\right)\frac{\partial\omega}{\partial x_i}\right]+2\rho(1 - F_1)\sigma_{\omega2}\frac{1}{\omega}\frac{\partial k}{\partial x_i}\frac{\partial\omega}{\partial x_i} \quad (10)$$

where γ is a function of Menter's blending function $\gamma=0.46\,F_1+0.44(1-F_1)$ and σ_ω is a function defined by Menter $\sigma_\omega=\sigma_{\omega1}F_1+\sigma_{\omega2}(1-F_1)$ where $\sigma_{\omega1}=0.65$, $\sigma_{\omega2}=0.856$ are calibrated by Menter for the *k-ω* SST model.

4.1. Discretization method

A commercial finite volume method (FVM) is used to solve the Reynolds momentum equation of the *k-ω* SST model, the turbulent kinetic energy equation of the *k-ω* SST model, used one of pressure-velocity coupling methods SIMPLE (Semi-Implicit Method for Pressure-Linked Equations) for the continuity and the velocity depends on the pressure gradient or, when discretized, on the difference between pressure values ½ cell either side. Computation was carried out to start first by solving the mass conservation, the Reynolds momentum equation of the *k-ω* SST model equations to determine the air flow characteristics and the flow field in the computational domain. CFD codes provide a variety of face interpolation scheme to calculate the face value U_f. When we setting up CFD code and we choosing Second-order / Liner Upwind a discretization scheme to put the method of interpolating the flow variables on the cell faces given the values of the cell centroids. These schemes calculate the face value (f) from the owner (P) and neighbor (N) cell centroids. The choice of turbulence model can affect solution accuracy. The k-ω SST model performs better than the stander and RNG k-epsilon models. The time step size for transient simulation was 0.002s and number of time steps 500 and 10 iterations that also affect the solution accuracy. Special care has to be taken on this aspect of a CFD code and pressure-velocity algorithms have been subject of continuously revised guidelines over the years. Coupled with the Finite Volume (FVM) discretization technique, the Semi-Implicit Method for Pressure-Linked Equations (SIMPLE) and its derivatives have become one of the most popular methods for solving the incompressible Navier-Stokes equations. The fig. 3 below shows flowchart of The SIMPLE algorithm.

4.2. Mesh sensitivity analysis

Before delving into the results extraction, it is wise to check the numerical solution from the point of mesh accuracy and how it relates to the mesh density. A. mesh sensitivity analysis was performed for eight different sizes. The first one contained 629,390 elements, the second 757,643, the third 972,686, the fourth 1,052,664, the fifth 1,180,478, the sixth 1,386,772, the seventh, 1,597,566, and the eighth 1,782,660. The element sizes for the eight meshes are 0.5, 0.4, 0.32, 0.3, 0.275, 0.245, 0.245, 0.225, and 0.21 m, respectively. Evaluate eight different meshes under steady-state conditions with a constant inlet airflow of 0.00204 kg.s^{-1}.

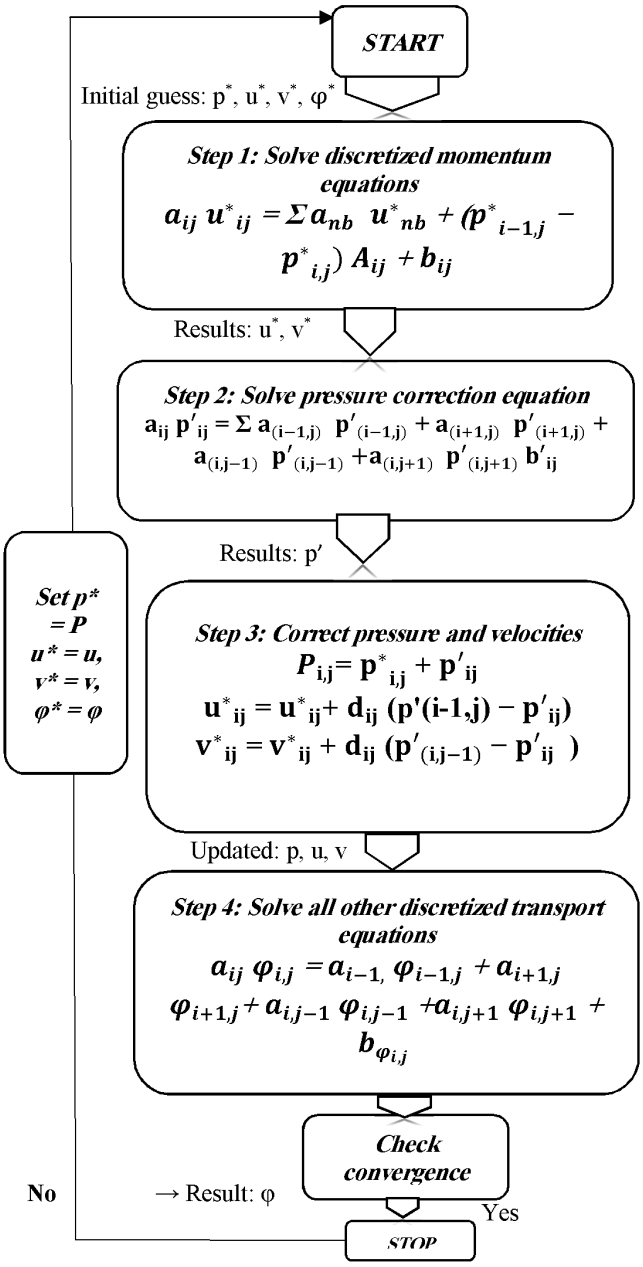

Fig. 3 The SIMPLE algorithm flowchart.

Table 1. The election of the most suitable mesh.

No.	Element size	Number of elements	Differential Pressure (Pa)
G1	0.5	629,390	6903.1006
G2	0.4	757,643	6721.3013
G3	0.32	972,686	6778.2319
G4	0.3	1,052,664	6800.7461
G5	0.275	1,180,478	6749.2871
G6	0.245	1,386,772	6770.5244
G7	0.225	1,597,566	6750.4517
G8	0.21	1,782,660	6772.3438

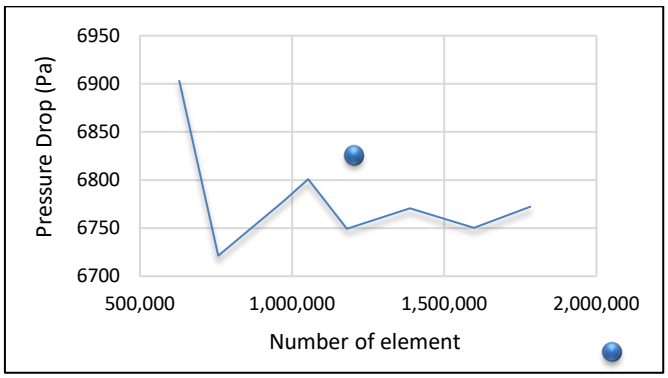

Fig. 4 The variation of the pressure drop with several mesh sizes.

4.3. Mesh deformation

Deformation methods are categorized into two types: physical analogy-based methods and interpolation-based methods. Basically, the physical analogy approaches treat the mesh deformation problem as a physical process that can be modeled using numerical methods. These approaches are accurate, reliable, and can be case-optimized by changing the physical parameters. However, in the interpolation-based approaches, an interpolation function is used to transfer prescribed boundary point displacements to the fluid mesh. These approaches are fast, easy to implement, and stable. Most of the FSI problems that are currently under investigation are considered very complicated and large. The mesh moves according to the bend in the membrane of the orifice, as shown in Fig. 5, which depicts the mesh deformation of a flow meter with a trapezoidal variable orifice at three different times.

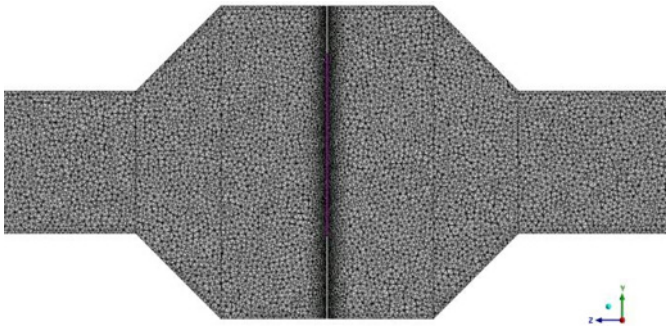

t = 0 sec

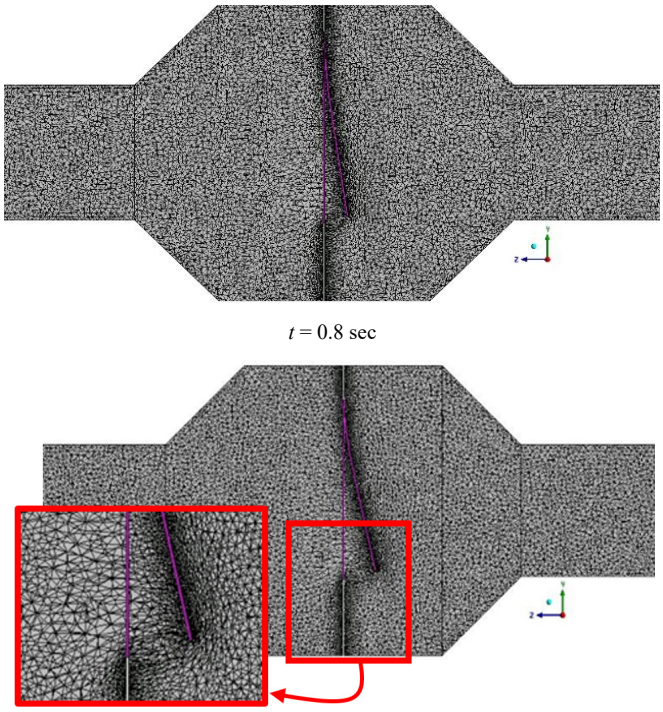

t = 0.8 sec

t = 1 sec

Fig. 5 Mesh deformation of the trapezoidal variable orifice flow meter at different times.

5. FSI formulations

The snapshot of the fluid-structure interaction is illustrated in Fig. 6. The fluid solver to calculate velocity and pressure is conducted first in each iteration using the Dirichlet condition. The traction of fluid acting on the solid wall is computed using the computed velocity and pressure. This traction is the Neumann boundary condition for a solid solver. A convergence check is performed for displacement at the interface. The solution is convergence when this displacement is not changed with the previous iteration, and the next time step is carried out. Otherwise, the process is continued and repeated for the next iteration.

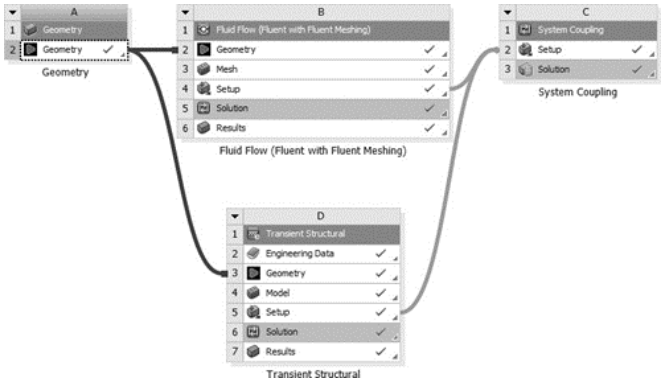

Fig. 6 snapshot of FSI coupling method.

5.1. CFD model validation

The validity of the present numerical analysis has been done by comparing the current CFD results with the results obtained by the experimental results of Martínez et al. [28] of variable orifice meter which were cut on Mylar sheets of elasticity modulus of $E = 2 \times 10^{10}$ N/m^2 and a cutting thickness of 0.7 mm and orifice thickness of 0.1 mm. Figure 7 illustrates the sketches of the resolved problem of [28], which is composed of a rectangular flexible membrane. Table 2 observed that for the mesh studied, the agreement between present numerical and experimental values of deflection is reasonably good. On the basis of this comparison, it is adequate to ensure accurate computation.

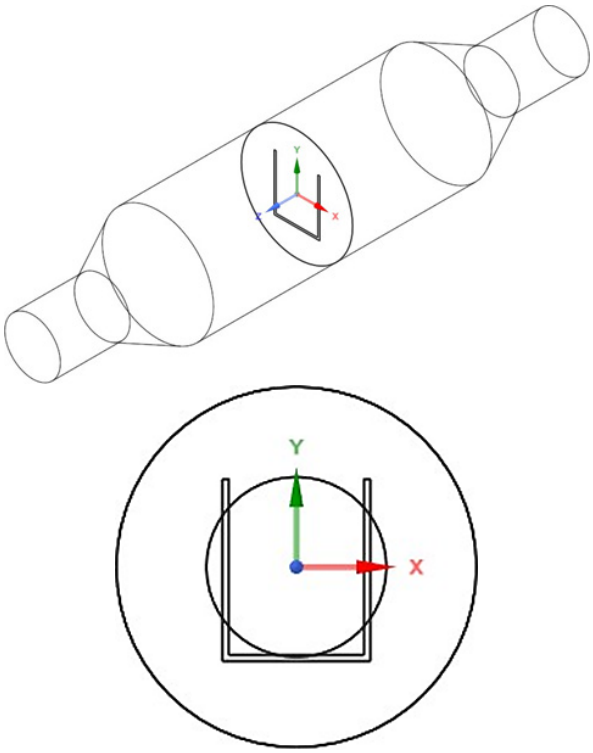

Fig. 7 The geometry of the variable area orifice utilized in validation with Martínez's et al experimental paper [28].

Table 2. Comparison between the deflection of the present numerical solution and experimental results of Martínez et al. [28].

Experimental results of Martínez et al. [28]			Present results
(L/min)	(kg/s)	Yr (mm)	Y (mm)
4.2	0.00008575	0.1	0.04455
11.9	0.00024296	0.2	0.36041
21.3	0.00043488	0.4	0.72521
31	0.00063292	0.8	1.0445
40.6	0.00082892	1.2	1.3169
51.2	0.00104533	1.5	1.5932
61.2	0.00124950	1.9	1.8328
71.6	0.00146183	2.2	2.0858
81.2	0.00165783	2.7	2.3106
89.3	0.00182321	3.1	2.4685

6. Results and discussion

The outcomes of the numerical modelling of the flow through the VOFM are presented in this section. The numerical analysis was projected on a trapezoidal flexible membrane. The transient results are assessed by displaying the distribution of the velocity and the deflection of the trapezoidal flexible membrane and the associated stress with time. At steady states, the results are portrayed by assessing the extent of the membrane deflection and the associated pressure drop with various mass flow rates.

6.1. Flow visualization

Figure 8 presents the velocity contours of a trapezoid within a longitudinal plane (along the z-axis) extracted four times every 0.1 s, the membrane deflects to permit more flow of air until it reaches maximum deflection at t = 1 sec. The chamber occupying the variable orifice manifests various velocity statuses: low velocity magnitude at the upstream near-wall regions and different velocity distributions at the downstream region. This indicates the formation of eddies behind the flexible membrane.

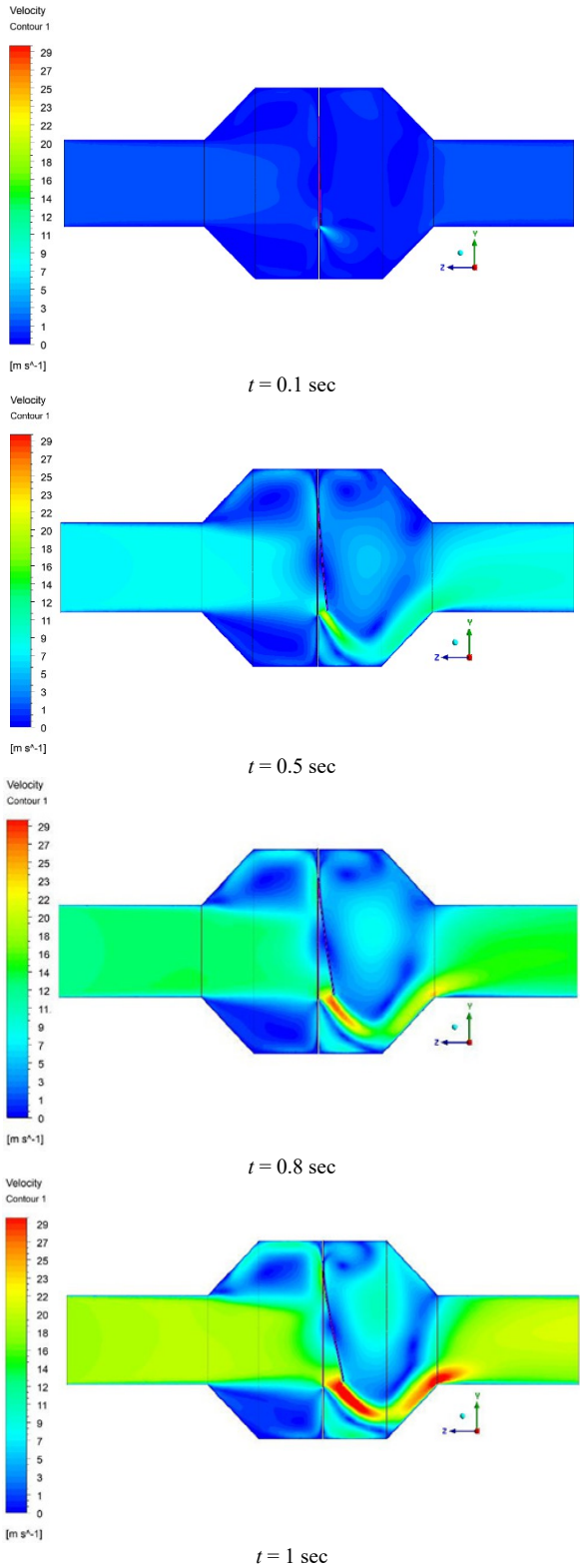

Fig. 8 Velocity distribution with different time.

The vertex of a trapezoidal membrane indicates the maximum velocity. For the same arrangement. Downstream of the flexible membrane, the altered flow patterns and asymmetric velocity fields signify vortex shedding and wake creation. The eddies, produced by sudden expansion and membrane-induced disturbances, promote mixing but may also bring unsteady flow behaviors that could affect pressure recovery and system efficiency. Additionally, the low-velocity areas upstream, particularly adjacent to the wall limits, indicate the formation of boundary layers and zones of flow separation. Such effects are characteristic of interior flows with intricate geometries and adaptable boundaries, where viscous forces and inertial effects contend, resulting in spatial fluctuations in the velocity field.

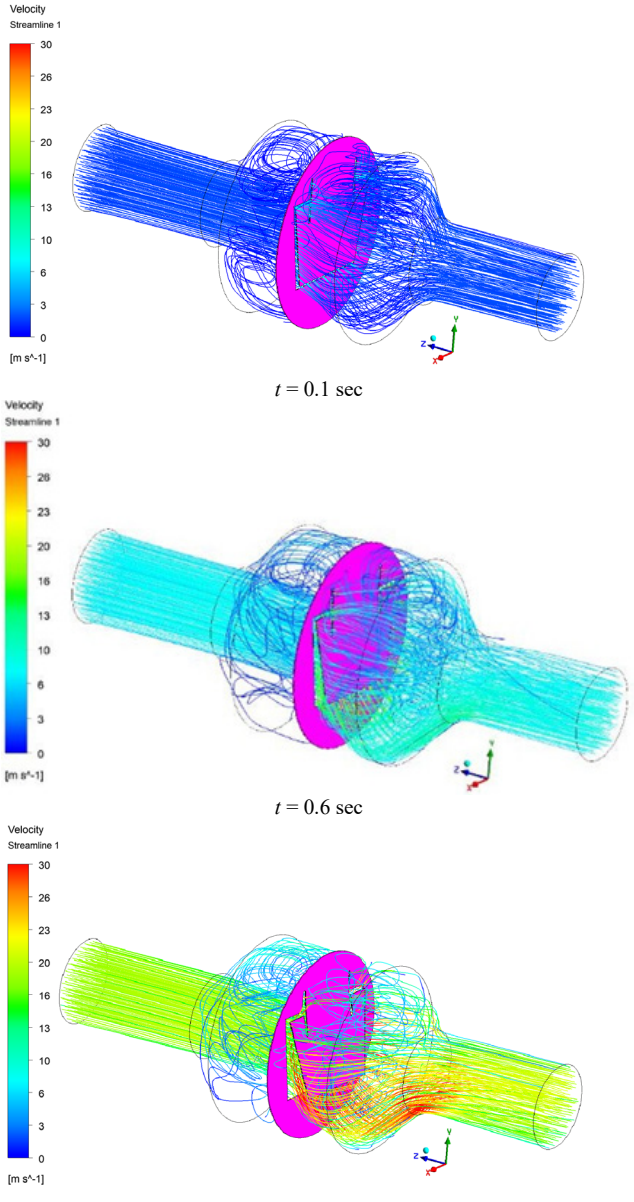

Fig. 9 stream lines with different time.

The distribution of the pressure along the flowmeter z-axis is depicted in Fig. 10 for a trapezoidal extracted for each 0.1 s with four times. The figure reveals that the upstream regions of a trapezoidal remain with constant positive pressure and along the various times. Downstream of the orifice, the pressure exhibits notable variations with time. The minimum

negative pressures are indicated just downstream the edges of the membrane where the velocity there is maximum. It is worth to indicated that the efforts of researches and designers is to reduce the pressure fluctuations at this region to avoid excessive pressure drop which may add a resistance to the breathing of patients who using ventilators. The overall pressure drop will be examined in the next sections.

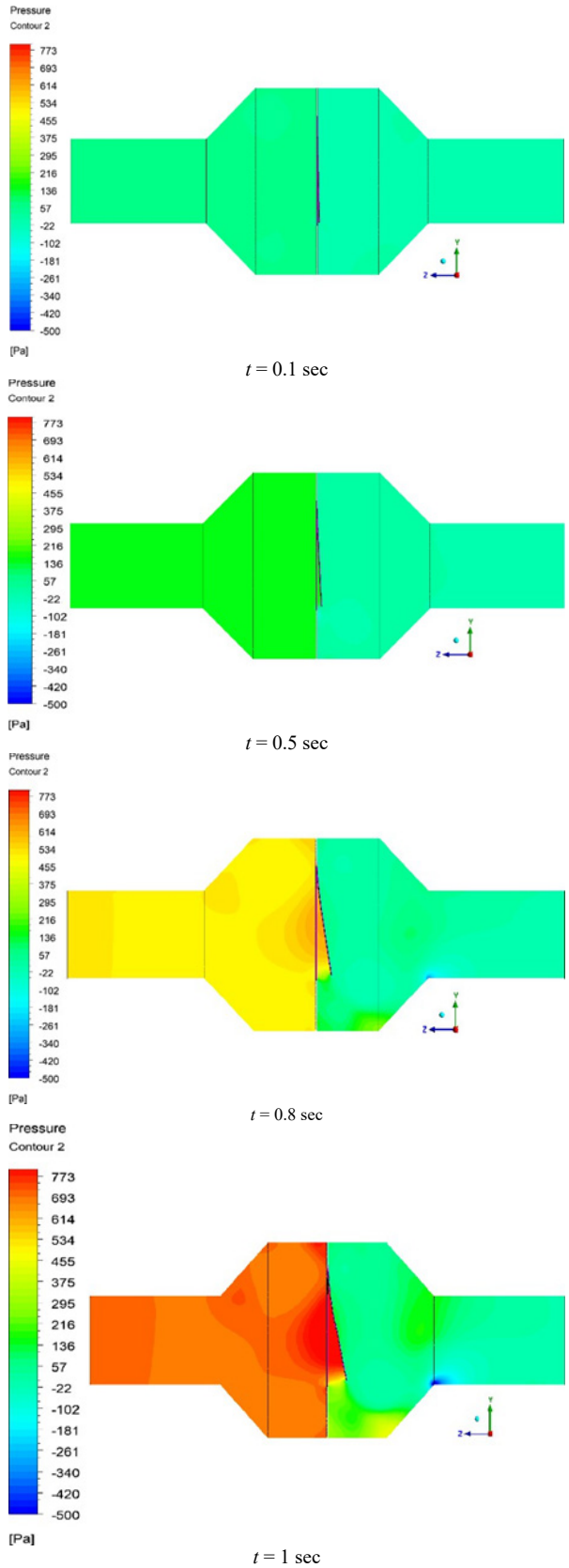

Fig. 10 Pressure distribution along z-axis.

6.2. Stress assessment

To assess the life cycles of the flowmeter, it is necessary to examine the stress distribution within the membrane. Figure 11 portrays the stress distribution at four times for a trapezoidal membrane. At an early time, where the deflection in the membrane is ignorable, there is no significant stress; however, at t = 1 sec, the deflected membrane indicates a significant stress concentration at the fixing boundary. This result tells that the deformation of the membrane is pivotal rather than continuous deformation. The illustration illustrates that maximal stress is localized near the edge of the circular orifice, where airflow pressure is greatest or where geometric discontinuities exist. The maximum Von Mises stress is approximately 153 MPa at 1 second, remaining below the yield strength of Mylar, indicating that the sensor structure can withstand the pressure without incurring irreparable damage. The remainder of the sensor body exhibits very low stress levels, indicating a consistent and mechanically robust construction. These findings validate the structural integrity of the flow sensor under standard airflow circumstances.

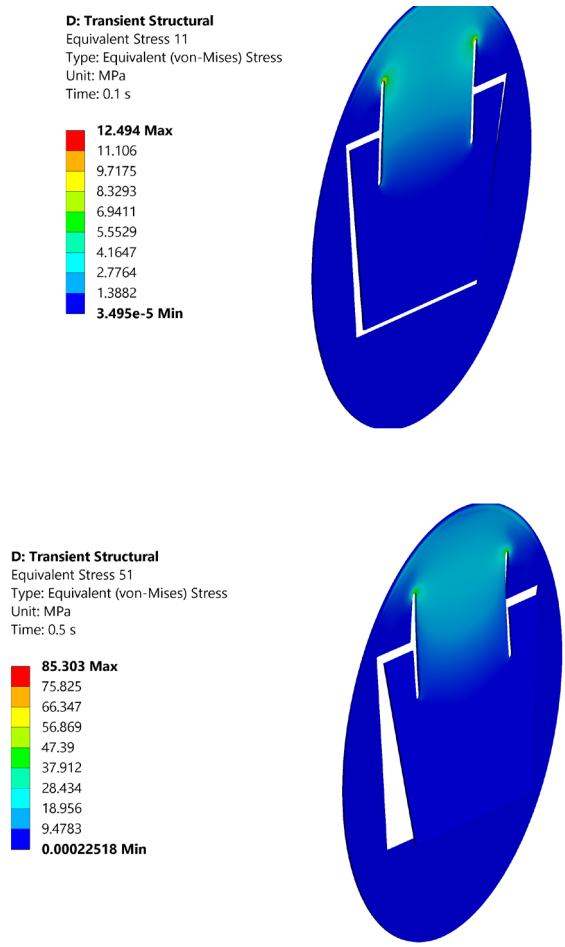

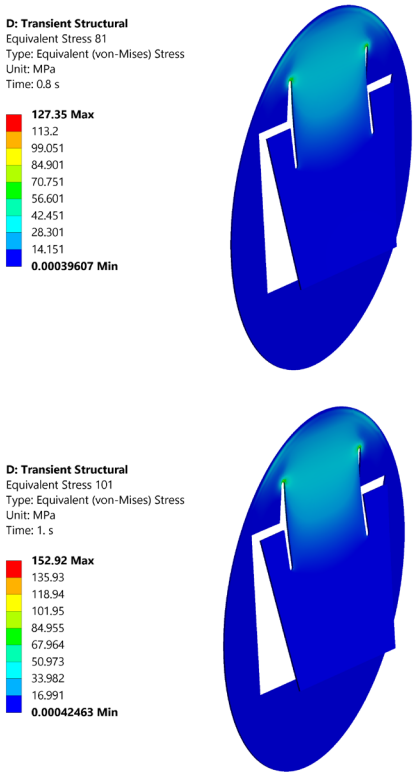

Fig. 11 Stress distribution on trapezoidal variable orifice plate at different times.

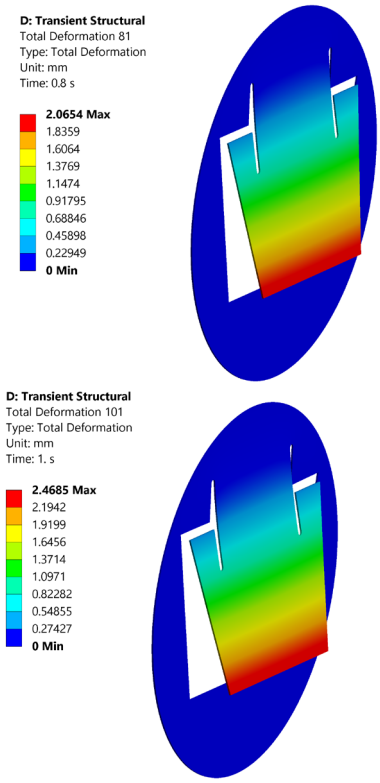

Fig. 12 Total deformation of trapezoidal variable orifice plate at different times.

6.3. Deformation assessment

Figure 12 portrays the quantified deformation in a trapezoidal model at four times. At t = 1 s, the figure shows maximum deflection at the vertex of a trapezoidal membrane. It is a reasonable result, where the strain in thin material is obviously greater than the thick material. In some of the next figure, the displacement will be presented with the various mass flow rates.

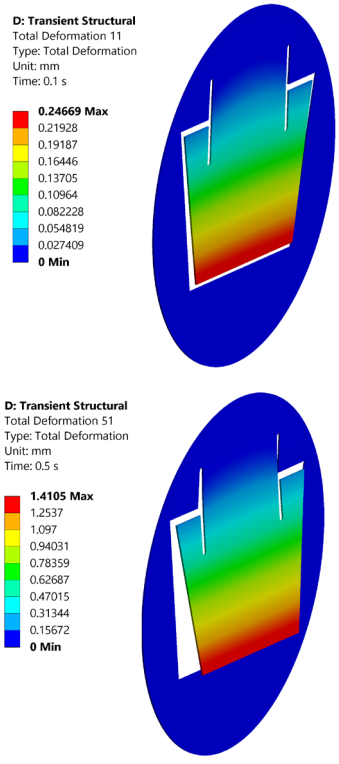

6.4. Displacement

An increase in the thickness of the VOFM results in less deflection and a smaller opening for fluid passage, increasing the flow resistance. This accounts the importance of thickness in the design and operation of variable orifice meters. Figure 13 displays the high sensitivity of the flowmeter

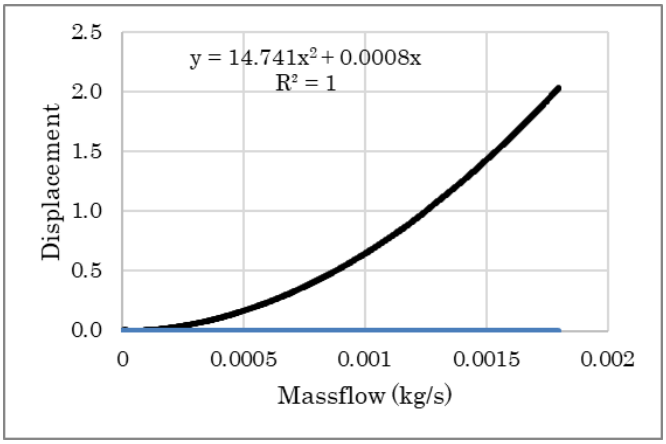

Fig. 13 Displacement of the trapezoidal variable orifice flow meter with the mass flow rate.

6.5. Pressure difference

The relationship between pressure difference and flow rate is intricate and interconnected. As flow rate increases, pressure drop tends to rise as well, primarily due to increased friction between the fluid and the conduit walls. Conversely, decreasing the flow rate can lead to a reduction in pressure drop. as shown in Fig. 14. This finding can be used in selection of proper orifice plate geometry for relevant industrial applications.

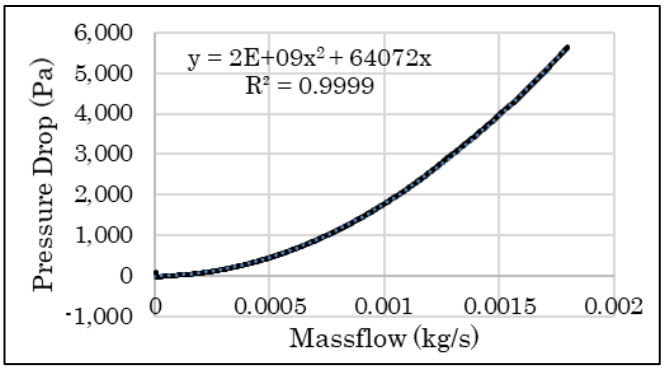

Fig. 14 Variation of the pressure drop with the mass flowrate.

6.6. Drag coefficient

The graph presented in Fig. 15 shows the relationship between mass flow rate and drag coefficient. This graph is critical for understanding how changes in the mass flow rate influence the drag coefficient. As the mass flow rate increases, the drag coefficient initially rises due to increased resistance encountered by the airflow within the system. However, beyond a certain point, the drag coefficient may plateau or even decrease, indicating an optimized flow condition where the ventilator operates efficiently. This relationship is essential for optimizing ventilator settings to ensure effective air delivery with minimal resistance, enhancing patient comfort and respiratory support.

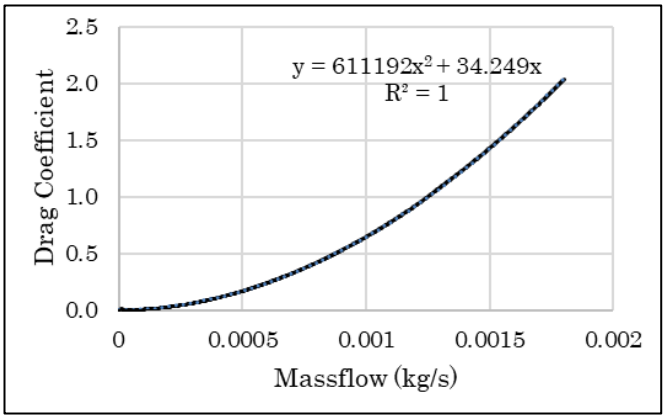

Fig. 15 Drag coefficient variation with the mass flow rate.

7. Conclusions

The present paper develops a mathematical description and a numerical solution of a trapezoidal variable orifice flow meters (VOFM). This type of flowmeter is vital instrument accompanied in the mechanical ventilators. The numerical solution was validated with previous experimental results by Martínez et al. [28] and its outcomes are trusted. This result highlights the importance of thickness in the design and operation of variable orifice meters. In general, an increase in VOFM thickness results in decreased deflection and a lower flow aperture, hence enhancing flow resistance. Consequently, augmenting the thickness requires an elevated flow rate for the changeover. The relationship between deflection and mass flow rate explored to determine how different rates affect the overall displacement of the membrane. It is expected that higher mass flow rates will result in greater deflection due to the increased strain on the material. These findings will provide valuable insights into the behavior of trapezoidal membranes under varying conditions of mass flow.

8. Recommendations

This study presented the results of a numerical analysis focused on a flowmeter utilizing a variable trapezoidal orifice. This work examined other experimental research particularly that of Martínez et al. used the rectangular shape of variable orifice flow meters. Future studies should employ diverse geometries and an expanded array of sheet materials with varying thicknesses of the flexible membrane. We suggest investigating the design of a variable diameter orifice, specifically focusing on circular and elliptical geometries, to assess their impact on flow characteristics. This design would enable the orifice to automatically increase, decrease, or completely close off based on specific flow conditions or the patient's medical needs. Additionally, using smart algorithms or ANN for control could help make better decisions about changing the orifice size to manage flow more effectively. It is recommended to test the system in changing conditions and analyze how temperature and fluid humidity affect it to make it more practical and reliable.

Nomenclature		
Symbol	**Description**	**SI Units**
v	Fluid velocity vector (u, v, w)	m/s
C	Flow coefficient	-----
CD	Drag coefficient	-----
p	pressure	N/m^2
f_b	Body force	N/m^3
t	Time	s
k	Turbulent kinetic energy	m^2/s^2
q_m	Mass flow rate	kg/s
u_i	Velocity component in direction i	m/s
x, y	Cartesian coordinate	-----
i, j	Count (1, 2, 3)	-----
t	Turbulent	-----
in	Inlet	-----
$\|\Omega\|$	Magnitude of the vorticity vector	-----
Greek symbols		
Symbol	**Description**	**SI Units**
β^*	Model constant (Wilcox's constant)	-----
ω	Specific dissipation rate	1/s
μ	Air dynamic viscosity	kg/m.s
ρ	Air density	kg/m^3
σ_k	Blended turbulent diffusion coefficient for k	-----
υt	Turbulent kinematic viscosity	m^2/s
μ_t	Turbulent viscosity	kg/m.s

References

[1] J. H. T. Bates, M. J. Turner, C. J. Lanteri, B. Jonson and P. D. Sly, Measurement of flow and volume, John Wiley & Sons, ISNB 978-0471184399, 1996.

[2] W. Ganong, Medical Physiology, Manual Moderno, ISBN 970729063X, 1999.

[3] L. P. Boulet, P. M. O'Byrne, "Asthma and exercise-induced bronchoconstriction in athletes", The New England Journal of Medicine, Vol. 372, No. 7, pp. 641-648, 2015. https://doi.org/10.1056/NEJMra1407552

[4] S. Cecchini, E. Schena, M. Notaro, M. Carassiti, and S. Silvestri, "Non-invasive estimation of cardiac output in mechanically ventilated patients: a prolonged expiration method", Annals of Biomedical Engineering, Vol. 40, No. 8, pp. 1777–1789, 2012. https://doi.org/10.1007/s10439-012-0534-3

[5] P. J. Peyton, D. Thompson, and P. Junor, "Non-invasive automated measurement of cardiac output during stable cardiac surgery using a fully integrated differential CO_2 Fick method", Journal of Clinical Monitoring and Computing, Vol. 22, No. 7, pp. 285-292, 2008. https://doi.org/10.1007/s10877-008-9131-2

[6] R. W. Miller, Introduction to the differential producer, Flow Measurement Engineering Handbook, 1996.

[7] G. L. Morrison, D. Terracina, C. Brewer, and K. R. Hall, "Response of a slotted orifice flow meter to an air/water mixture," Flow Measurement and Instrumentation, Vol. 12, No. 3, pp. 175-180, 2001. https://doi.org/10.1016/S0955-5986(01)00018-8

[8] J. J. Osborn, "Variable orifice gas flow sensing head", US Patent 4,083,245, United States Patent and Trademark Office, 1978. https://patents.google.com/patent/US4083245

[9] D. W. Guillaume, M. G. Norton, and D. F. DeVries, "Variable orifice flow sensing apparatus", US Patent 4,993,269, United States Patent and Trademark Office, 1991. https://patents.google.com/patent/US4993269

[10] J. Stupecky, "Variable area obstruction gas flow meter", US Patent 5,083,621, United States Patent and Trademark Office, 1991. https://patents.google.com/patent/US5083621

[11] J. J. Osborne, "Fluid flow meter", US Patent 4,083,246, United States Patent and Trademark Office, 11 April 1978. https://www.freepatentsonline.com/4083246.pdf

[12] R. J. Mears, "Fluid flow meter with variable area obstruction", US Patent 4,006,634, United States Patent and Trademark Office, 8 February 1977. https://patents.google.com/patent/US4006634A/en

[13] D. W. Guillaume, M. G. Norton, and D. F. DeVries, "Variable orifice flow sensing apparatus", US Patent 4,993,269, United States Patent and Trademark Office, 16 Dec.1988. https://patents.google.com/patent/US4993269

[14] G. Tardi, C. Massaroni, P. Saccomandi, and E. Schena, "Experimental Assessment of a Variable Orifice Flowmeter for Respiratory Monitoring", Journal of Sensors, Vol. 2015, Issue 1, Article ID 752540, 2015. https://doi.org/10.1155/2015/752540

[15] F. Montagna, E. Schena, C. Massaroni, C. Caciotti, D. L. Presti, and S. Silvestri, "Influence of the Length of Lead Lines on the Response of a Variable Orifice Meter: Analysis of Sensitivity and Settling Time", IEEE, International Symposium on Medical Measurements and Applications, 2018. https://doi.org/10.1109/MeMeA.2018.8438738

[16] E. Schena, G. Lupi, S. Cecchini, and S. Silvestri, "Linearity dependence on oxygen fraction and gas temperature of a novel Fleisch pneumotachograph for neonatal ventilation at low flow rates", Measurement, Vol. 45, No. 8, pp. 2064–2071, 2012. https://doi.org/10.1016/j.measurement.2012.05.009

[17] E. Schena, S. Cecchini, and S. Silvestri, "An orifice meter for bidirectional air flow measurements: Influence of gas thermo-hygrometric content on static response and bidirectionality", Flow Measurement and Instrumentation, Vol. 34, pp. 105-112, 2013. https://doi.org/10.1016/j.flowmeasinst.2013.09.001

[18] A. A. E-A. Aly, A. Chong, F. Nicolleau, S. Beck, "Experimental study of the pressure drop after fractal-shaped orifices in turbulent pipe flows", Experimental Thermal and Fluid Science, Vol. 34, No. 1, pp. 104-111, 2010. https://doi.org/10.1016/j.expthermflusci.2009.09.008

[19] G. L. Morrison, K. R. Hall, J. C. Holste, M. L. Macek, L. M. Ihfe, R. E. DeOtte Jr., D. P. Terracina, "Comparison of orifice and slotted plate flowmeters", Flow Measurement and Instrumentation, Vol. 5, No. 2, pp. 71-77, 1994. https://doi.org/10.1016/0955-5986(94)90039-6

[20] R. H. M. D. Beer, M. H. Kuypers, J. Holland, and H. Schotte, "Flow Resistance Tube for Gas Flow Meter", EP Patent EP0331772A1, 1989. https://patents.google.com/patent/EP0331772A1/en

[21] J. Bonassa, "Flow Sensor with Double Obstruction", US Patent US20090064794A1, United States Patent and Trademark Office, 2010. https://patents.google.com/patent/US20090064794A1/en

[22] H. Friberg and J. Daescher, "Respiratory Flow Sensor", US Patent US10905357B2, United States Patent and Trademark Office, 2021. https://patents.google.com/patent/US10905357B2/en

[23] F. Moukalled, L. Mangani, and M. Darwish, Erratum to: The Finite Volume Method in Computational Fluid Dynamics, springer, ISBN978-3-319-16873-9, 2016.

[24] DuPont Teijin Films, Mylar® Product Information Bulletin: H-37232-3, DuPont Teijin Films, 2003. https://www.dupontteijinfilms.com

[25] F. R. Menter, "Improved two-equation Eddy-viscosity turbulence models for engineering applications", AIAA Journal, Vol. 32, No. 8, pp. 1598-1605, 1994. https://doi.org/10.2514/3.12149

[26] D. Agoropoulos and L. C. Squire, "The reassessment of the scale-determining equation for advanced turbulence models", AIAA Journal, Vol. 26, No. 10, pp. 1299-1310, 1988. https://doi.org/10.2514/3.10028

[27] B. E. Launder and D. B. Spalding, "The numerical computation of turbulent flows", Computer Methods in Applied Mechanics and Engineering, Vol. 3, Issue 2, pp. 269-289, 1974. https://doi.org/10.1016/0045-7825(74)90029-2

[28] W. P. Martínez, J. F. A. Londoño, and J. V. Gómez, "Design and Construction of a Device to Evaluate the Performance of Variable Orifice Flow Meters (VOFM)", Inventions, Vol. 8, No. 5, 2023. https://doi.org/10.3390/inventions8050110